

Article

Transport Properties of Nanostructured Li_2TiO_3 Anode Material Synthesized by Hydrothermal Method

Ambadi Lakshmi-Narayana ¹, Obili M. Hussain ¹, Alain Mauger ² and Christian M. Julien ^{2,*} 

¹ Thin Films Laboratory, Department of Physics, Sri Venkateswara University, Tirupati 517502, India; Inarayan37@gmail.com (A.L.-N.); hussainsvu@gmail.com (O.M.H.)

² Sorbonne Université, Campus Pierre et Marie Curie, Institut de Minéralogie, de Physique des Matériaux et de Cosmochimie (IMPMC), CNRS UMR 7590, 4 place Jussieu, 75005 Paris, France; Alain.mauger@upmc.fr

* Correspondence: christian.julien@upmc.fr

Received: 25 June 2019; Accepted: 4 July 2019; Published: 20 September 2019

First Version Published: 10 July 2019 (doi:10.3390/sci1020039)

Second Version Published: 20 September 2019 (doi:10.3390/sci1030056)



Abstract: Li_2TiO_3 nanopowders were synthesized by hydrothermal process using anatase TiO_2 and $\text{LiOH}\cdot\text{H}_2\text{O}$ as raw materials. Li_2TiO_3 crystallizes in the layered monoclinic structure (space group $C2/c$) with average crystallite size of 34 nm. Morphology, elemental composition and local structure of products were carried out using high-resolution transmission electron microscopy, field-emission scanning electron microscopy, Raman and Fourier transform infrared spectroscopy. Transport properties investigated by d.c. (4-probe measurements) and a.c. (complex impedance spectroscopy) show the activation energy of 0.71 and 0.65 eV, respectively. The ionic transport properties of Li^+ ions in nanocrystalline Li_2TiO_3 characterized by cyclic voltammetry and impedance spectroscopy validate the good electrochemical properties of this anode material for lithium-ion batteries.

Keywords: hydrothermal reaction; nanoparticles; Li_2TiO_3 ; anode; ionic transport; lithium batteries

1. Introduction

Among all titanium-based metal oxides, various members including TiO_2 rutile, TiO_2 anatase, $\text{TiO}_2(\text{B})$, LiTi_2O_4 , $\text{Li}_2\text{Ti}_3\text{O}_7$, Li_2TiO_3 , LiTiO_2 and $\text{Li}_4\text{Ti}_5\text{O}_{12}$ are considered as potential electrode materials for Li-ion batteries (see the phase diagram in Figure 1) [1–11]. In these compounds, the reversible intercalation/deintercalation process of lithium ions involves the reduction of Ti^{4+} to Ti^{3+} that takes place in safe voltage region (>0.5 V vs. Li^+/Li^0). This redox potential gives faster Li^+ charging and sustainable cyclability to the electrode because of the congruence to the lowest unoccupied molecular orbital (LUMO) of the organic liquid-carbonate electrolyte, thus avoiding the formation of electrode/electrolyte interphase [12].

Among all titanium-based metal oxides, the rock-salt lithium metatitanate Li_2TiO_3 is an important material in various energy-related applications including lithium-ion batteries and molten carbonate fuel cells, due to its higher and flatter potential profile for lithium insertion preventing the formation of Li dendrites and the decomposition of electrolyte as well. The crystal structure was determined and refined by several workers [13–15]. Li_2TiO_3 exists in three polymorphic structures: the metastable cubic phase $\alpha\text{-Li}_2\text{TiO}_3$ (space group $Fm\bar{3}m$), which transforms above 300°C to the stable framework $\beta\text{-Li}_2\text{TiO}_3$ and the high-temperature cubic $\gamma\text{-Li}_2\text{TiO}_3$ phase formed at 1155°C (space group $Fm\bar{3}m$) [16,17]. Since, we are concerned with applications of the material near room temperature, attention is focused hereunder on the stable phase $\beta\text{-Li}_2\text{TiO}_3$.

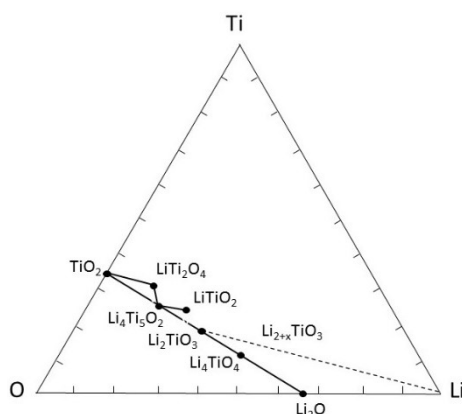


Figure 1. Ternary Li-Ti-O phase diagram showing the lithiation path of Li_2TiO_3 (dashed line).

The crystal structure of β -phase Li_2TiO_3 was first determined by Lang [18] and subsequently refined by Kataoka et al. [19]. It can be described by the chemical formula $\text{Li}_{4/3}\text{Ti}_{2/3}\text{O}_2$ or layered notation $\text{Li}(\text{Li}_{1/3}\text{Ti}_{2/3})\text{O}_2$ and crystallizes in the rock-salt monoclinic structure (space group $C2/c$) [18]. The unit cell has twenty-four atoms with lattice parameters $a = 5.0622 \text{ \AA}$, $b = 8.7712 \text{ \AA}$ and $c = 9.74787 \text{ \AA}$, $\alpha = 90^\circ$, $\beta = 100.01^\circ$ and $\gamma = 90^\circ$ [19–21]. Both Li and Ti cations are located in octahedral sites with three crystallographically inequivalent Li positions, namely Li(1), Li(2) and Li(3), occupying the $8f$, $4d$ and $4e$ Wyckoff sites, respectively, while two non-equivalent titanium positions Ti(1) and Ti(2) reside on $4e$ sites. β - Li_2TiO_3 has a layered-type framework that is a stacking of LiTi_2 layers composed of Li(3) and Ti cations sharing $4e$ position and of single Li layers fully occupied by Li(1) and Li(2) ions [22,23].

Various synthesis methods have been reported to grow nanocrystalline Li_2TiO_3 . Conventional solid-state synthesis reaction was used to produce Li_2TiO_3 with the mixture of Li_2CO_3 and TiO_2 at 900 – $1100 \text{ }^\circ\text{C}$ for 10 h to several days [21,24–26]. Other preparation methods such as wet-chemical methods include sol-gel technique [27], combustion method [28,29], polymer solution synthesis [30], ball milling [31,32] and extrusion-spheronisation sintering [33] that involve at least one high temperature step (over $900 \text{ }^\circ\text{C}$) to obtain a well-crystallized Li_2TiO_3 phase (named LTO hereafter). To the best of our knowledge, only few reports are available on hydrothermal synthesis of Li_2TiO_3 using micro-sized TiO_2 powder as raw material [17]. Uniform nano- Li_2TiO_3 powder particles were prepared via a cetyltrimethyl-ammonium bromide (CTAB)-assisted hydrothermal method [34]. Unlike many synthesis methods, the hydrothermal method allows the control of shape and size of the particles by control of the rate of precipitation of the crystallized powders directly from the solution, the uniformity of nucleation, growth and aging. Expensive surfactants or template are not necessary in this method. Thus, hydrothermal synthesis is a suitable method to produce large scale crystals with high quality at a reasonable price [35].

However, β - Li_2TiO_3 is a wide gap semiconductor with an indirect band gap at Γ -C ($E_g \approx 3.9 \text{ eV}$) with low electrical conductivity of $10^{-11} \text{ S cm}^{-1}$ at room temperature [35–37] and it was considered as a material with electrochemical inactiveness similarly to the rock-salt Li_2MnO_3 [38]. However, synthesis of nanocrystalline LTO, under the form of nanoparticles, nanorods, nanoflowers and nanofibers, provides more active surface area and shorter diffusion paths for Li^+ ions in the structure, which makes the material electrochemically active and improves the rate capability [39,40]. Several attempts on Li_2TiO_3 -based composites as cathode or anode materials were reported considering the merits of lithium metatitanate, namely its excellent structural stability and improved electrochemical performance for Li-ion batteries [41–47]. The Si/LTO nanocomposite synthesized by sol-gel process as an anode material exhibited a specific capacity of 471 mAh g^{-1} even after 50 cycles. In this nanocomposite, the structural stability is due to Li_2TiO_3 , which acts as excellent buffer to the Si powders and partly compensates the capacity loss [44]. The composite $0.55\text{Li}_2\text{TiO}_3$ - 0.45LiCrO_2 prepared by spray pyrolysis exhibits the highest initial discharge capacity of 203 mAh g^{-1} [45]. Due to its three-dimensional (3D) path for

Li⁺-ion migration and its excellent structural stability, LTO has served as both a Li ion conductive layer and a protective coating layer of cathode material against the attack of HF in the electrolyte [48–52].

In previous works, we have investigated the electrochemical properties of pristine nano-LTO [53], and the improve performance of LTO/CNT and LTO/graphene composites [54]. The effect of nanosized Li₂TiO₃ was evidenced by the excellent cyclability and the stable specific discharge capacity of 113, 143 and 150 mAh g⁻¹, respectively, retained over 30 charge–discharge cycles at 1C rate. In the present study, we report additional measurements that evidence the beneficial effect of nanosized scale on the transport properties of LTO specimens prepared by hydrothermal synthesis after heat treatment at 800 °C in ambient conditions. The transport properties are investigated using d.c. and a.c. electrical conductivity, cyclic voltammetry (CV) and electrochemical impedance spectroscopy (EIS). Finally, the structural stability and the cyclability of LTO nanopowders cycled in aqueous cell is discussed.

2. Materials and Methods

2.1. Synthesis

Nanocrystalline β-Li₂TiO₃ was synthesized by hydrothermal reaction using 1.198 g (0.015 mol) TiO₂ powder (anatase phase, Sigma-Aldrich, USA) and 1.259 g (0.03 mol) LiOH·H₂O (Sigma-Aldrich, USA) as raw materials. TiO₂ and LiOH·H₂O powders (molar ratio 2:1) were added into a Teflon lined autoclave (50 mL) together with 15 mL distilled water and heated at 200 °C for 10 h. During the reaction period the autoclave was kept at the autogenous saturation vapor pressure of the solution without agitation. Then, the product was filtered, rinsed with deionized water. The as-prepared powder was dried at 50 °C in ambient conditions. The obtained powder was calcined at 800 °C for 2 h in air.

2.2. Characterization

The structure of samples was investigated by the X-ray diffraction (XRD) technique using a Siefert computerized X-ray diffractometer (model 3003-TT) equipped with a CuK_α radiation (λ = 1.5406 Å) source filtered by Ni film operated at a scan speed of 0.03 degree per second in the 2θ range 10°–70°. Raman scattering (RS) spectra were recorded at room temperature in the range of 50–1000 cm⁻¹ with a spectral resolution of ≈1 cm⁻¹ using a HR800UV Raman spectrometer (Jobin-Yvon, Longjumeau, France) using air-cooled frequency doubled Nd:YAG laser 532 nm with an excitation source of 50 mW. The spectral calibration was carried out using the 520 cm⁻¹ scattering line of silicon. A 100× objective lens was used to focus the laser light on sample surface. The Fourier transform infrared (FTIR) measurements were carried out using a VERTEX 80v (Bruker, Karlsruhe, Germany) in the spectral range 100–1000 cm⁻¹. High resolution transmission electron microscope (HRTEM) (model FEI, TECHNAI G²-30 S-twin D905) was used to analyze the microstructure of the sample. The surface morphology of the sample was observed by a field emission scanning electron microscope (FESEM, SIRION 200). The composition of the sample was analyzed by energy dispersive spectroscopy with FESEM (FESEM, SIRION 200).

A.C. conductivity was performed by impedance spectroscopy using a phase sensitive multimeter (model PSM 1700, Newton, Leicester, UK) at various temperatures from 300 to 500 °C. The amplitude of the A.C. signal was 50 mV over the frequency range 1 Hz–1 MHz. The synthesized powder was pressed into 12 mm diameter pellet with the thickness of 1.25 mm and annealed at 600 °C for 2 h to enhance the packing density. The pellet was used for electrical studies. Cyclic voltammetry (CV), galvanostatic charge–discharge experiments were conducted to evaluate the specific discharge capacity of the electrode as reported elsewhere [54]. A conventional three-electrode glass cell (Pt/saturated Li₂SO₄ aqueous solution/Li₂TiO₃) was used with an Ag/AgCl reference electrodes.

3. Results

3.1. Elemental and Structural Studies

The elemental analysis of the as-prepared Li_2TiO_3 powders sintered at $800\text{ }^\circ\text{C}$ for 2 h carried out by energy dispersive spectroscopy (EDS) gives the composition of 74.5 and 25.5% (accuracy of $\pm 0.5\%$) of titanium and oxygen, respectively (see Figure 2 in Ref. [54]). The LTO samples have a white color, which indicates a stoichiometric composition, according to Hoshino et al. [55] for products sintered in oxidizing conditions.

Figure 2b presents the XRD pattern of Li_2TiO_3 sample recorded using the Bragg–Brentano geometry. All the X-ray diffraction lines can be readily indexed to the monoclinic $\beta\text{-Li}_2\text{TiO}_3$ structure (JCPDS Card No. 33-0831). The XRD diagram exhibits predominant (002) reflection at $2\theta = 18.48^\circ$ along with other characteristic orientations ($\bar{1}31$), ($\bar{1}33$), (043), (006), (312) and (062) corresponding to monoclinic $\beta\text{-Li}_2\text{TiO}_3$ structure with $C2/c$ space group (ordered phase). In the hydrothermal reaction, the Li-Ti-O framework is formed, characterized by the basic ($\bar{1}33$) lattice plane. The strong intensity of ($\bar{1}33$) diffraction peak gives evidence of the good ordering of lithium and titanium ions in the LiTi_2 slab of the monoclinic structure in which Li, Ti and O atoms are arranged in the sequence $\text{Li}_{\text{interslab}}(\text{Li}_{1/3}\text{Ti}_{2/3})_{\text{slab}}\text{O}_2$. In this lattice, lithium ions occupy $1/3$ of $4e$ sites, while the titanium ions occupy $2/3$ other $4e$ sites (Wyckoff notation) [37]. Note that the intensity of the (002) supercell XRD peak is enhanced by the sintering process at $800\text{ }^\circ\text{C}$ for 2 h. Rietveld refinements of XRD data were performed by the FULLPROF program [56]. The comparison between observed (dots) and calculated (solid line) patterns is shown in Figure 2 together with their difference curve. The lattice parameters of the monoclinic structure (space group $C2/c$) are $a = 5.069(1)\text{ \AA}$, $b = 8.799(1)\text{ \AA}$, $c = 9.759(2)\text{ \AA}$ and $\beta = 102^\circ$. The elementary unit volume ($V = abc \sin\beta$) is 429.1 \AA^3 . These results match well with the literature data and confirm that the specimens are single Li_2TiO_3 phase [15–17]. The crystallite size of the prepared sample was estimated using Debye–Scherrer formula [57]:

$$L = \frac{K\lambda}{\beta \cos \theta} \quad (1)$$

where β is the full width half maxima (FWHM) in radians, λ is wavelength of the X-ray, θ is corresponding Bragg angle and K is a dimensionless shape factor ($K = 0.94$). The estimated crystallite size is $34 \pm 2\text{ nm}$ with a lattice strain 0.009 in the rock-salt Li_2TiO_3 powders.

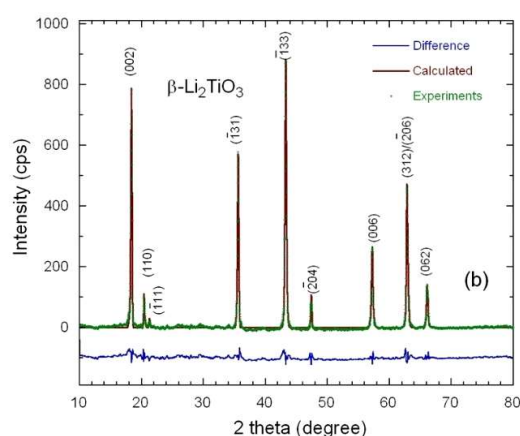


Figure 2. X-ray diffraction pattern of Li_2TiO_3 powders indexed in the monoclinic symmetry, $C2/c$ space group of the $\beta\text{-Li}_2\text{TiO}_3$ phase. The Rietveld refinement is shown with $\chi^2 = 5.21$.

The short-range structural properties of the prepared samples were further investigated by Raman and FTIR spectroscopy that are considered to be powerful for either detecting impurities or determine the local environment of oxygen atoms. In lithiated oxides, where Li ions occupy octahedral sites,

the frequency of Li-O stretching is known to be observed within the 200–400 cm^{-1} spectral region, while for Li tetrahedrally coordination, the frequency lies in the 400–550 cm^{-1} region [58]. Figure 3a shows the Raman spectra in the spectral range 100–900 cm^{-1} of several titanate oxides, i.e., TiO_2 anatase, TiO_2 rutile, $\text{Li}_4\text{Ti}_5\text{O}_{12}$ spinel and $\beta\text{-Li}_2\text{TiO}_3$, which evidence the unicity of the monoclinic structure of Li_2TiO_3 . Among the 15 allowed Raman active modes ($7A_g + 8B_g$) of the C_{2h}^6 spectroscopic symmetry, only 11 observed Raman bands are observed, which can be attributed as followed. The high-wavenumber peaks at 575 and 668 cm^{-1} are assigned to the Ti-O stretching vibrations in TiO_6 octahedra; the lattice modes, i.e., $A_g(\text{T})$ translational lattice mode, and O-Ti-O bending modes appear at $\nu < 320 \text{ cm}^{-1}$; the low-frequency peak at 98 cm^{-1} (with very weak intensity) is due to the Li-O stretching modes in LiO_4 and LiO_6 are observed at 358 and 430 cm^{-1} , respectively. Frequency and intensity of Raman bands are listed in Table 1. Our data are in good agreement with the literature [21,36,59–63]. Recently, Raman and infrared bands of Li_2TiO_3 have been calculated by Wan et al. [36] from first-principles total energy calculations with a generalized gradient approximation and plane-wave pseudopotential model. Our experimental data are compared with calculated frequencies in Table 2. Note that similar situation has been shown in the Raman spectrum of monoclinic Li_2MnO_3 [64,65]. All mode frequencies match well with the relation:

$$\frac{\omega_{\text{Li}_2\text{TiO}_3}}{\omega_{\text{Li}_2\text{MnO}_3}} = \sqrt{\frac{m_{\text{Mn}}}{m_{\text{Ti}}}} \quad (2)$$

Considering the molecular model, the Raman spectrum of the $\beta\text{-Li}_2\text{TiO}_3$ phase essentially displays stretching and bending of the various polyhedral units constituting the monoclinic lattice without appearance of Raman bands due to anatase TiO_2 (at 144 cm^{-1}) and rutile TiO_2 (at 449/610 cm^{-1}).

The FTIR spectrum of Li_2TiO_3 is shown in Figure 3b. It displays only 9 infrared bands instead of 18 expected by the group factor analysis. The two broad peaks at 510 and 619 cm^{-1} are assigned to the antisymmetric stretching vibrations of Ti-O bonds. The low-frequency bands in the range 350–450 cm^{-1} are a mixture of the O-Li-O and O-Ti-O bending modes due to the presence of Li ions in the LiTi_2 slabs. The band at 263 cm^{-1} is attributed to the stretching mode of Li-O bonds in LiO_6 octahedra. The shoulder of the higher intensity peak at 642 cm^{-1} should be related to the local distortion of the lattice that results in a decrease of the local structural symmetry generating additional infrared bands [66].

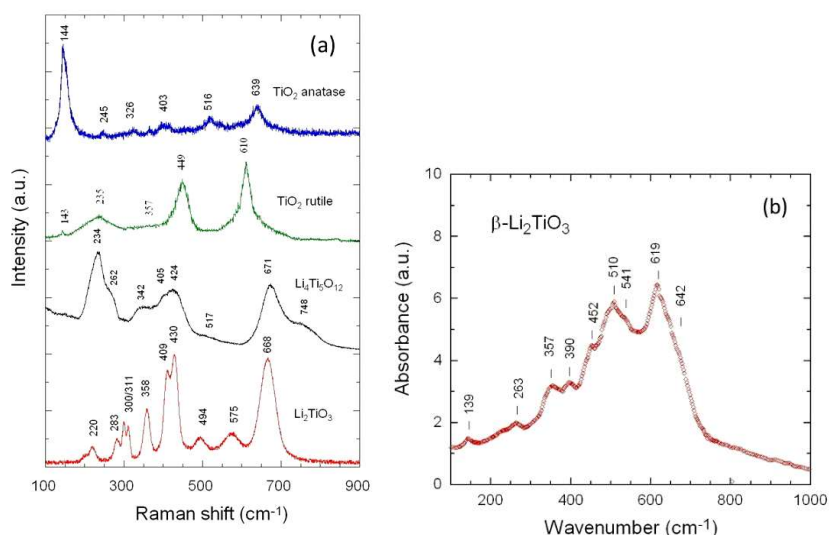


Figure 3. (a) Raman spectra of titanate compounds: anatase TiO_2 , rutile TiO_2 , spinel $\text{Li}_4\text{Ti}_5\text{O}_{12}$ and Li_2TiO_3 . (b) FTIR spectrum of Li_2TiO_3 recorded in the spectral range 100–1000 cm^{-1} at 2 cm^{-1} spectral resolution.

Table 1. Frequency (in cm^{-1}) and strength of Raman and infrared bands of $\beta\text{-Li}_2\text{TiO}_3$. Calculated frequencies are reproduced from Wan et al. [36].

Raman				Infrared			
$\omega_{\text{exp.}}$	Intensity *	$\omega_{\text{cal.}}$		$\omega_{\text{exp.}}$	Intensity *	$\omega_{\text{cal.}}$	
98	vw	83	A_g				
211	w	214	A_g	139	vw	143	B_U
277	m	278	B_g	266	vw	263	B_U
294	m	302	A_g	357	m	355	A_U
303	m	314	B_g	390	w	393	A_U
350	m	360	A_g	452	w	456	A_U
402	S	401	A_g	510	S	-	
420	S	432	B_g	541	m	544	B_U
484	w	470	B_g	619	S	617	A_U
567	w	542	A_g	642	s	634	A_U
658	S	617	A_g				

* w = weak, vw = very weak, m = medium, S = strong, s = shoulder.

3.2. Surface Morphology

The surface morphology and microstructural features of hydrothermal synthesized Li_2TiO_3 material calcined at 800°C for 2 h are observed by field emission scanning electron microscopy (FESEM) and high-resolution transmission electron microscope (HRTEM) in Figures 4 and 4b, respectively. FESEM image of Li_2TiO_3 shown in Figure 4a reveals that the sample consists of homogeneously distributed spherical-like shaped grains with an average particle size of 150 nm without any obvious aggregations. Figure 4b–d show the HRTEM image, selected area diffraction pattern (SAED) and lattice fringes images of Li_2TiO_3 , respectively. The corresponding selected-area electron diffraction (SAED) pattern of the microstructure (Figure 4c) shows that the nanoparticles are well crystallized. The d -spacing values obtained from SAED patterns are indexed to the respective planes of (002), ($\bar{1}$ 31), ($\bar{1}$ 33) and (312) that agree well with XRD patterns of the monoclinic structure of Li_2TiO_3 . Figure 2d shows the layered structure with fringe spacing of 0.48 nm matching well with the d -spacing of the high intensity plane (002) of Li_2TiO_3 and corresponding to LiTi_2 slab along the c -axis [67].

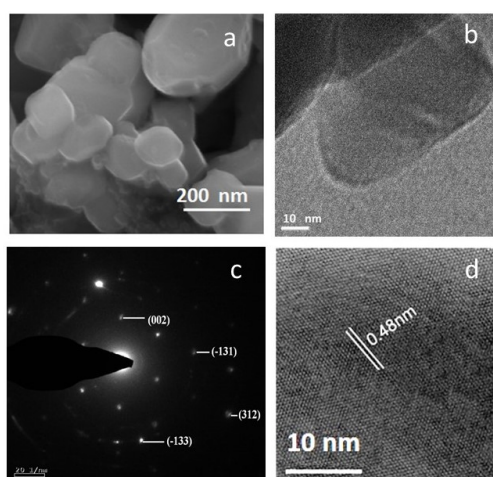


Figure 4. Morphology of nano Li_2TiO_3 (a) FESEM image showing spherical-like shaped grains with an average particle size of 150 nm. (b) HRTEM image, (c) selected area diffraction pattern (SAED) and (d) lattice fringes images of Li_2TiO_3 .

3.3. Electrical Transport

Conductivity measurements were carried out using both d.c. and a.c. techniques to analyze the electrical transport of electrons and ions in the LTO lattice. Impedance spectroscopy is an efficient tool

to study a.c. conductivity of materials, when using a large frequency domain, this technique provides analysis of intragrain, intergrain and relaxation process in material (Figure 5a–e). Figure 5a,b show the Nyquist plots ($Z'(\omega)$ - $Z''(\omega)$ plane) of nanocrystalline Li_2TiO_3 in a wide frequency range (1 Hz-1 MHz) over the temperature range 320–500 °C. The bulk resistance (R_b) of the LTO sample is determined from the intercept of each semicircle with the real axis. It is observed that both the intercept with the Z' axis and the maximum of Z'' shift as temperature increases. At low temperatures ($T < 400$ °C), the Li_2TiO_3 pellet exhibits a high resistance that is mainly due to the bulk property of the sample. At higher temperature, all the Nyquist plots consist of a slightly depressed semicircle in the high-frequency region followed by another depressed semicircle at low frequencies (<1000 Hz). The depressed semicircle, which meets real axis at high frequencies is the response of the bulk resistance (R_b) of the material, i.e., small deviation from a Debye-type relaxation process, while the depressed semicircle originated in the low frequency region is due to grain boundary (R_{gb}) effect. The high- and low-frequency complex impedance plots for all temperatures can be modeled using a parallel combination of resistance and constant phase element (CPE) equivalent circuit describing the bulk resistance and grain boundary components in Li_2TiO_3 sample. The bulk electrical conductivity (σ) was calculated using the formula:

$$\sigma_0 = \frac{1}{R_b} \times \frac{l}{S} \quad (3)$$

where R_b is the bulk resistance, l is the thickness of the sample and S is the active area of the sample.

The real $Z'(\omega)$ and imaginary $Z''(\omega)$ part of the Li_2TiO_3 sample impedance are presented for all temperatures in Figure 5c,d, respectively. The plots of Figure 5c show a decrease of $Z'(\omega)$ vs. frequency, so that $\sigma(\omega)$ increases with frequency (see Figure 5e). At low frequency, σ increases importantly with temperature. At high frequencies, however, $Z'(\omega)$ becomes almost temperature independent so that the $Z'(\omega)$ curves at different temperatures merge approximately in a single curve. This is due to the release of space charges caused by reduction in barrier properties of the material [38]. This unique curve at high frequency shows a dip, which is associated to charge carrier hopping in the material. In another hand, $Z'' = \text{Im}(Z(\omega))$ reaches a maximum, which shifts towards higher frequency with temperature. This is attributed to the active conduction through the grain boundaries of the sample. The magnitude of $Z''(\omega)$ decreases with increasing temperature indicating a decrease of the resistivity of the material. The peak broadening observed with increasing temperature is attributed to a temperature dependent relaxation process in the material. The asymmetric broadening of the peaks indicates the spread of relaxation time in the sample. Our data match well with the results reported in the literature [37,38,68]. The ac response obeys the power law [69]:

$$\sigma(\omega) = \sigma_{ac} = \sigma_0 + A\omega^n \quad (4)$$

where σ_0 is the d.c. conductivity (at $\omega = 0$), A is a thermally activated quantity and n the fractional constant that is $0.5 < n < 0.8$ for an ionic conductor [70,71]. The frequency exponent n (Equation (4)) can be analyzed by a mechanism based on charge carrier hopping between defect sites proposed by Elliott [72]:

$$n = \frac{\partial(\ln \sigma_{ac})}{\partial(\ln \omega)} = 1 - \frac{6k_B T}{W_m} \quad (5)$$

where T is the absolute temperature, k_B the Boltzmann constant and W_m the maximum barrier height (energy of the transport charge). Using Equation (4), from the slope of curves in Figure 5d, one can derive at the highest frequency with $n \approx 0.72$ and the value of W_m is 0.63 eV at room temperature.

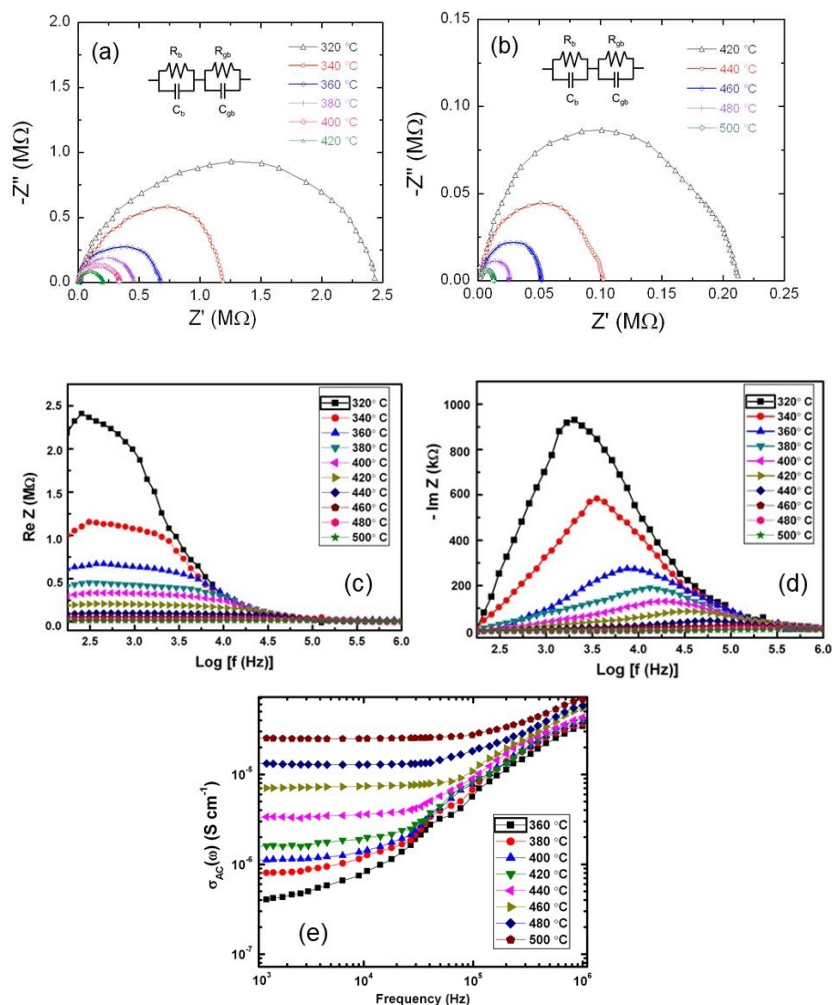


Figure 5. Temperature dependence of the electrical properties of nano-Li₂TiO₃. Nyquist plots of nanocrystalline Li₂TiO₃ in the temperature range 320–420 °C (a) and 420–500 °C (b). Variation of real part of the impedance $Z'' = \text{Re}(Z)$ vs. frequency (c). Variation of imaginary part of the impedance $Z'' = \text{Im}(Z)$ vs. frequency (d). Plot of the ac conductivity $\sigma_{ac}(\omega)$ versus frequency in the temperature range 360–500 °C (e).

Figure 6a,b display the Arrhenius plots of σ_{ac} and σ_{dc} , respectively. The solid lines are the fit of the temperature dependence of conductivity thermally activated according the Arrhenius-type behavior:

$$\sigma_{ac,dc} = \sigma_0 T \exp\left(\frac{-E_a}{k_B T}\right) \tag{6}$$

where σ_0 is the pre-exponential factor, T the absolute temperature, k_B the Boltzmann constant and E_{ac} the activation energy of the conductivity. The fit of the curves σT vs. $1/T$ in Figure 6a,b provides an activation energy $E_a = 0.71$ eV for σ_{dc} and 0.65 eV for σ_{ac} measured at 50 kHz. These values match well with the value 0.77 eV found for nanoparticles [37], against 0.88 eV [38] or even 0.95 eV for the bulk material [37]. Thus, E_a appears to be dependent on the crystallite size. This is corroborated by the fact that the value $E_a = 0.71$ eV obtained in the present work (34 nm crystallite size) is slightly smaller than that for crystallites of 88 nm reported by Dash et al. [38]. Therefore, nanosized particle favors the electronic transport and thus the ionic transport since both are correlated to maintain the electrical charge neutrality inside the material.

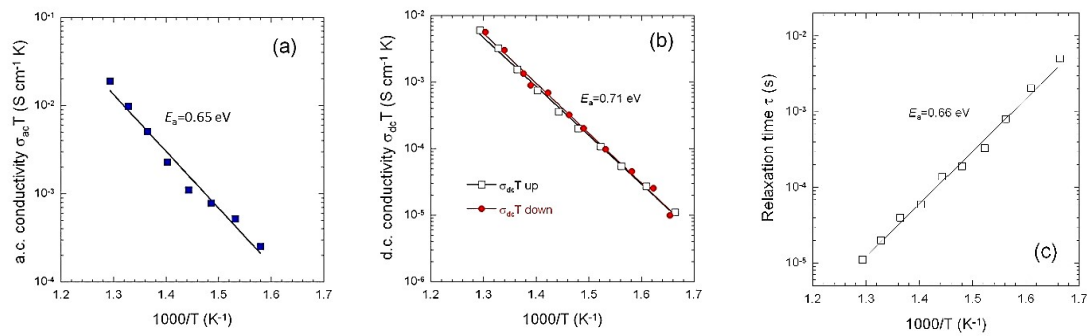


Figure 6. Temperature dependence of (a) a.c. conductivity measured at 50 kHz, (b) d.c. conductivity and (c) relaxation time.

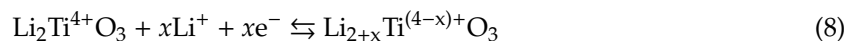
As shown in Figure 5c, $Z'' = \text{Im}(Z(\omega))$ exhibits a peak at the particular frequency, i.e., the relaxation frequency, which corresponds to a single relaxation time that fulfils the relation $2\pi f_m \tau_m = 1$, where f_m is the frequency of the maximum of $\text{Im}(Z)$. The variation of τ with T obeys an Arrhenius law given by [73]:

$$\tau = \tau_0 \exp\left(\frac{-W_a}{k_B T}\right) \tag{7}$$

where τ_0 is the pre-exponential factor and W_a the activation energy. Figure 6c shows the temperature dependence of the relaxation time of LTO sample in the range 320–500 °C. The mean relaxation time of the process is measured in fractions of milliseconds that does not implies electronic and ionic lattice polarization but slow relaxation can be imposed by permanent molecular dipoles, ion defects of a dipolar type, or mobile hopping charge carriers [74]. The activation energy estimated from the linear fit is found to be ~0.66 eV, which indicates a quasi-Debye behavior of the relaxation process of charge carriers in the LTO lattice. The mechanism of ionic motion has been discussed by several workers [23,74,75]. Li_2TiO_3 has a three-dimensional path for Li^+ ion diffusion, in which the ionic migration can occur in the (00*l*) plane, that is, LiTi_2 layer, and along the *c* axis [74]. The conductivity occurs with the hopping of Li^+ ions from tetrahedral sites to adjacent octahedral sites. At low temperatures, defects are created by surface modification. At high temperature a drift of large number of Li^+ ions released from tetrahedral sites (LiTi_2 layer) then occupied octahedral sites (Li layer), creating interstitial site vacancies that are thermally activated and some structural disorder possibly occurred that facilitate ion transport induced by low activation energy.

3.4. Li^+ -ion Diffusivity

Investigations of the diffusivity of Li^+ ions in the LTO lattice were carried out by cyclic voltammetry (CV) at sweep rate in the range 1–50 mV s^{-1} and by electrochemical impedance spectroscopy (EIS) measurements in the frequency range 1– 10^6 Hz for Pt/saturated Li_2SO_4 aqueous solution/ Li_2TiO_3 cells. Cyclic voltammograms display one set of well-defined current peaks (see Figure 7 in Ref. [53]) corresponding to the redox reaction in $\text{Li}/\text{Li}_2\text{TiO}_3$ cell, according the (de)insertion reaction:



As the starting electrode material is $\text{Li}_2^+\text{Ti}^{4+}\text{O}_3$, the insertion of the fraction *x* of Li^+ ions in $\text{Li}_{2+x}\text{TiO}_3$ implies the reduction of tetravalent to trivalent titanium [45]. At sweep rate of 10 mV s^{-1} , the reduction peak occurred at 0.338 V during cathodic sweep corresponding to insertion of lithium into interstitial sites of $\text{Li}_{2+x}\text{TiO}_3$ (*x* equals to 0.5), while the oxidation peak occurred at 0.643 V during anodic sweep. Thus, a peak separation of 0.305 V for Li_2TiO_3 is ascribed to the Li^+ ion storage at the solid–electrolyte interface during charge–discharge process [76].

Figure 7a displays the dependency of the peak current *I_p* for the redox peaks as a function of scan rate *v* in CV measurements (typical CV response at $v = 10 \text{ mV s}^{-1}$ is shown in the inset of Figure 7a).

For cathodic and anodic reactions, the plots in double logarithmic scale show mutual linear behavior over the entire measurement range with a slope of 0.511 and 0.497, respectively. These values are very close to 0.5, which characterizes the conventional diffusion-controlled faradaic reaction, i.e., the lithium insertion/extraction reaction in LTO. The classical Randles–Sevcik equation for a semi-infinite diffusion of Li-ion into Li_2TiO_2 layer can be applied [77]:

$$I_p = 0.446 \left[\frac{n^3 F^2 C_{\text{Li}}^2 A^2 D_{\text{Li}} \nu}{RT} \right]^{\frac{1}{2}} \tag{9}$$

where I_p is the peak current, n the charge-transfer number, A the surface area in cm^2 of the electrode, D_{Li} the chemical diffusion coefficient, ν the scan rate, C_{Li} the bulk concentration of Li-ion in electrode ($\sim 1.8 \times 10^{-3} \text{ mol cm}^{-3}$ calculated from the volume of Li_2TiO_3 (429.1 \AA^3)), F is Faraday constant, R the gas constant and T the absolute temperature. Based on Equation (9), the apparent diffusion coefficient of Li-ion in the nanostructured Li_2TiO_2 sample was calculated to be $9.2 \times 10^{-12} \text{ cm}^2 \text{ s}^{-1}$.

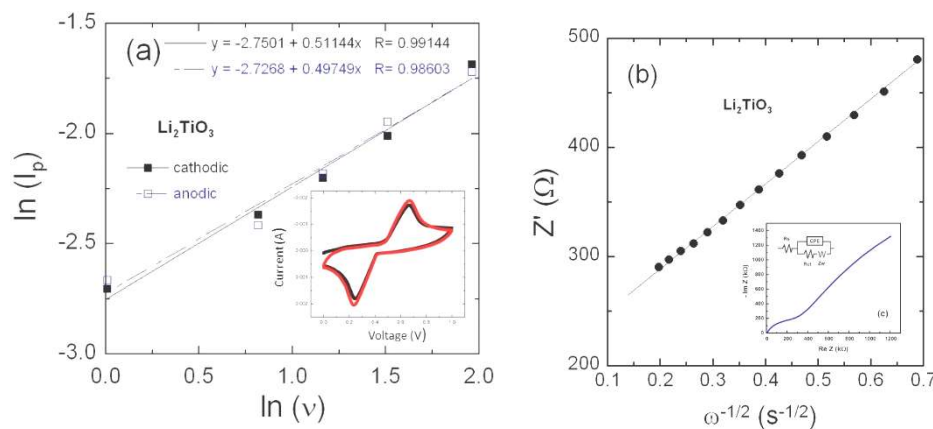


Figure 7. Determination of the Li^+ -ion transport in nano- Li_2TiO_3 . (a) Plot of $\ln(I_p)$ vs. $\ln(\nu)$ from CV data. Inset shows the typical CV response at 10 mV s^{-1} . (b) Plot of Z' vs. $\omega^{-1/2}$ plots in the Warburg region of the EIS shown in the inset.

Electrochemical impedance spectroscopy (EIS) was carried out over the frequency range from 1 Hz to 1 MHz for $\text{Li}_{2+x}\text{TiO}_3$ electrode in the fully charged state, i.e., $x(\text{Li}) = 0$. The Nyquist plot consists of a depressed semicircle in high frequency and straight line at low frequency region. The interception of Z' axis at high frequency indicating electrode/electrolyte contact resistance corresponds to the solution resistance (R_s). The depressed semicircle in the middle frequency region denotes the charge transfer resistance R_{ct} related to electrochemical reaction at electrode/electrolyte interface. At low frequency, the observed straight line that is the response of the Warburg impedance Z_w , which is related to solid-state diffusion of Li^+ ions. The impedance spectrum was fitted using the Randles equivalent circuit shown in the inset of Figure 7b. Resistance R_s of the electrode is $38 \text{ }\Omega$; R_{ct} is $\approx 250 \text{ }\Omega$ and slope of the Warburg impedance ($\theta \approx 45^\circ$) indicates that the electrode is controlled by a diffusion process. In the Warburg regime, the impedance varies with the angular frequency ω according to the law [78]:

$$Z' = R_s + R_{ct} + \sigma_w \omega^{-1/2} \tag{10}$$

in which the Warburg impedance σ_w is obtained from the slope of Z' vs. $\omega^{-1/2}$ in the low-frequency range (Figure 7b). The apparent diffusion coefficient Li^+ ions can be quantified from the low-frequency Warburg impedance according the equation [78]:

$$D_{\text{Li}^+} = \frac{1}{2} \left[\frac{RT}{F^2 A C_{\text{Li}} \sigma_w} \right]^2 \tag{11}$$

where R , T and F are the usual constants, A the surface area of the electrode-electrolyte interface and C_{Li} the lithium-ion concentration in the electrode. Linear fit of data in Figure 7b gives $\sigma_w = 9.36 \text{ V s}^{-1/2}$ and $D_{Li^+} = 2.1 \times 10^{-11} \text{ cm}^2 \text{ s}^{-1}$. Note that the D_{Li^+} (EIS) value is larger by a factor of 2 in comparison to that obtained by CV. Similar difference in D_{Li^+} for the same cathode material by two different techniques is commonly observed [79,80].

Figure 8a,b present the cyclability of the $\text{Li}_{2.55}\text{TiO}_3$ electrode (discharge state). The XRD patterns of the starting Li_2TiO_3 and final $\text{Li}_{2.55}\text{TiO}_3$ phase after cycling process are displayed in Figure 8a displays. These results show that the structure has retained after 30 insertion-extraction cycles with the $C2/c$ monoclinic symmetry. This insertion process is in good agreement with the model of Bian and Dong [59] who demonstrated the formation of a non-stoichiometric $\text{Li}_{2+x}\text{TiO}_3$ with $x = 0.2$ that retains the initial rock-salt structure. These authors have proposed three possible occupation mechanisms in Li-rich Li_2TiO_3 : (i) excess of Li^+ ions occupied the tetrahedral interstitial sites, which took the composition $\text{Li}_{2+4y}\text{Ti}_{1-y}\text{O}_3$; (ii) the Li^+ ions are located on the Ti^{4+} sites formed as antisite defects ($2\text{Li}''_{\text{Ti}} = 3\text{V}_\text{O}^{\bullet\bullet}$); and (iii) excess of Li^+ ions occupied itself site and Ti^{4+} and O^{2-} site vacancies formed simultaneously. The plot of the specific discharge capacity vs. cycle number for the Li_2TiO_3 electrode over 30 cycles in the voltage range 0.0–1.0 V is shown in Figure 5b. The Li_2TiO_3 anode exhibited an initial discharge capacity of $\approx 122 \text{ mAh g}^{-1}$ that is retained up to $\approx 114 \text{ mAh g}^{-1}$ after 30 cycles. The capacity retention is about 94%. In this figure the present results are compared with those of literature [41,43,46,47].

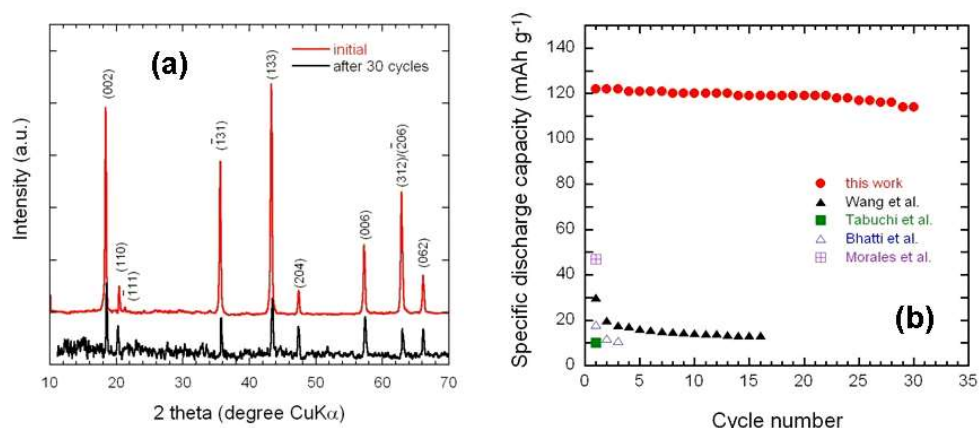


Figure 8. (a) XRD patterns of the starting Li_2TiO_3 and final $\text{Li}_{2.55}\text{TiO}_3$ phase after cycling process. (b) Specific discharge capacity vs. cycle number for the Li_2TiO_3 electrode over 30 cycles at $C/13$ rate.

4. Discussion

In view of these previous results reported in Figure 8b, one understands why Li_2TiO_3 was not considered as a possible anode element. Indeed, the material in these works were not investigated as an anode for itself, but was used as an element entering in the composition of a composite with another anode material, usually $\text{Li}_4\text{Ti}_5\text{O}_{12}$ [46,47], or LiFeO_2 [41,43]. Coating lamellar cathode element with Li_2TiO_3 has also been made [81]. In any case, the voltage range used for electrochemical investigation was 1–3 V, since $\text{Li}_4\text{Ti}_5\text{O}_{12}$ or LiFeO_2 or the lamellar compounds are active only at voltage higher than 1 volt. However, in the range 1–3 V, Li_2TiO_3 is simply electrochemically inactive. The purpose of the addition of Li_2TiO_3 in the composite was to increase the ionic conductivity and stabilize the structure of the electrode materials [46,48,81] by taking advantage of the strong Ti–O bond in Li_2TiO_3 [82–84]. In addition, Li_2TiO_3 is known to be a fast Li^+ conductor when it is doped [85,86]. Here, no doping has been made, but the conductivity has been improved owing to the nano-size of the particles. In the present work, we have shown that nanostructured Li_2TiO_3 has interesting electrochemical properties at low voltage ($< 1 \text{ V}$). This result can also explain former results obtained on $\text{Li}_4\text{Ti}_5\text{O}_{12}/\text{Li}_2\text{TiO}_3$ composite. In Ref. [47], the authors noticed an increased capacity of this composite, associated to a sloping

discharge in the range 1.25–0 V with respect to the results observed when cycling with a lower cut-off of 1.25 V. Although this effect was attributed to an intrinsic property of $\text{Li}_4\text{Ti}_5\text{O}_{12}$ since an increased capacity in this voltage range has been reported by one group with $\text{Li}_4\text{Ti}_5\text{O}_{12}$ alone [87], the present work suggests that at least part of this effect can be attributed to Li_2TiO_3 . In addition, the enhanced conductivity and the correlated improved Li-diffusion by reduction of the Li_2TiO_3 material to the nanosize observed in the present work explains the enhanced electrochemical performance of recent electrospun $\text{Li}_4\text{Ti}_5\text{O}_{12}/\text{Li}_2\text{TiO}_3$ composite nanofibers observed recently [88].

Table 2. Values of the activation energy for the charge carrier transport in Li_2TiO_3 reported in the literature.

Method Used	Activation Energy (eV)	Ref.
^7Li NMR, a.c. conductivity	0.47–0.80	[89]
a.c. conductivity	0.81–0.91	[90]
electrical conductivity	0.60–0.90	[37]
$^{6,7}\text{Li}$ NMR	0.27	[74]
periodic quantum–chemical DFT	0.44–0.54	[75]
complex impedance	0.77/0.88	[38]
d.c. conductivity	0.86	[68]
$^{6,7}\text{Li}$ NMR	0.52	[91]
atomistic simulation	0.51	[92]
DFT calculations	0.76	[93]
a.c. conductivity	0.65/0.71	this work

Few experimental works reported the kinetics of Li^+ ion in the LTO framework, while the Li ion dynamics is discussed controversially. Table 2 list the values of the activation energy for the charge carrier transport in Li_2TiO_3 reported in the literature. Vijayakumar et al. utilized a combination of $^{6,7}\text{Li}$ nuclear magnetic resonance (NMR) and molecular dynamics (MD) simulations to predict that Li ions can be occupy a tetrahedral site if a Ti cationic defect is present in the LiTi_2 layer. They obtained a small activation energy of 0.27 eV for Li diffusion in $\beta\text{-Li}_2\text{TiO}_3$, which seems to be associated with impurities and stoichiometric deviation [74]. Ruprecht et al. [89] reported a self-diffusion coefficient of $2 \times 10^{-13} \text{ cm}^2 \text{ s}^{-1}$ measured by ^7Li NMR stimulated echoes at 160 °C and an extremely slow Li diffusion, i.e., $D_{\text{Li}^+} = 3 \times 10^{-17} \text{ cm}^2 \text{ s}^{-1}$ at room temperature, evaluated from a.c. conductivity with the help of the Nernst-Einsten equation. Islam and Bredow [75] determined activation energies ranging between 0.44 and 0.55 eV for Li^+ ion migrating along the *ab* plane and perpendicularly to the LiTi_2 layers as well. The early work by Vitins et al. [90] shows that the electrical conductivity of Li_2TiO_3 is strongly dependent on the heat treatment conditions during sample preparation. Typical specimen mixed with 1.5 mol% Li^+ and annealed at 760 °C for 20 h exhibits a conductivity of $\sigma_{300} = 4 \times 10^{-6} \text{ S cm}^{-1}$ and $E_a = 0.81 \text{ eV}$ in the temperature range 187–424 °C. The authors suggested an excess TiO_2 incorporated in the lattice by $\text{Ti}_{\text{Li}}^{3+}$ defects charge compensated for by $\text{V}_{\text{Li}}^{-1}$ defects, which facilitates Li diffusion. Ruprecht et al. [89] reported a dc conductivity of 5×10^{-13} and $4 \times 10^{-6} \text{ S cm}^{-1}$ at room temperature and 250 °C, respectively (with $E_a = 0.8 \text{ eV}$ for long-range Li transport above 100 °C), which is very close with the value $3 \times 10^{-6} \text{ S cm}^{-1}$ at 300 °C obtained by Fehr and Schmidbauer [37]. Employing atomistic simulations to study the point defect processes and lithium diffusion in LTO, Kuganathan et al. evaluated the activation energy of 0.51 eV for Li^+ migration along the *ab* plane and showed that the energetically favorable intrinsic defect is lithium Frenkel type with 1.25 eV per defect [92]. More recently, Ki et al. considered three types of lithium vacancies to investigate the diffusion behavior of tritium in LTO using density functional theory (DFT) calculations and found a minimum energy barrier of 0.76 eV for the tritium atom to escape the Li vacancy well [93].

5. Conclusions

The nanocrystalline Li_2TiO_3 phase has been successfully synthesized using a simple, low cost and scalable hydrothermal reaction. The structural analyses carried out using X-ray diffraction, Raman and FTIR spectroscopy show that $\beta\text{-Li}_2\text{TiO}_3$ crystallizes with $C2/c$ space group with crystallites 34 nm. FESEM image shows that the nanocrystalline $\beta\text{-Li}_2\text{TiO}_3$ particles are homogeneously distributed as nearly spherical shaped grains with an average size of 150 nm. The Raman and FTIR spectroscopy confirm the impurity free monoclinic structure exhibiting well-defined vibrational modes Ti-O and Li-O stretching and O-Ti-O and O-Li-O bending modes. The electrical properties revealed a thermally activated conduction mechanism (Arrhenius-type behavior) with an activation energy of 0.71 eV. The conduction mechanism of the sample is greatly improved due to more charge carriers corresponding to nanoparticles. The electrochemical of $\beta\text{-Li}_2\text{TiO}_3$ studies demonstrate that reduction of $\text{Ti}^{4+}/\text{Ti}^{3+}$ (0.55 Li uptake) occurred in potential range 1.0–0.0 V. The nanocrystalline $\beta\text{-Li}_2\text{TiO}_3$ shows a specific discharge capacity of 114 mAh g^{-1} after 30 cycles at current density of 0.05 mAh cm^{-2} . These results suggest that nanocrystalline $\beta\text{-Li}_2\text{TiO}_3$ nano particles have shortened the Li-ion diffusion lengths and enhanced the electrochemical kinetics of the sample, which are very important keys to high rate capacity. The electrode retains 94% of capacity even after 30 cycles with an excellent structural stability.

Author Contributions: Conceptualization, O.M.H.; experimental, A.L.-N.; data analysis; C.M.J.; writing—review and editing, C.M.J. and A.M.

Funding: This work was supported by the Council of Scientific & Industrial Research (CSIR), India. Grant CSIR-UGC NET-JRF/SRF.

Conflicts of Interest: The authors declare no conflict of interest.

References

1. Julien, C.M.; Mauger, A.; Vijn, A.; Zaghbi, K. *Lithium Batteries: Science and Technology*; Springer: Cham, Switzerland, 2016.
2. Mauger, A.; Xie, H.; Julien, C.M. Composite anodes for lithium-ion batteries: Status and trends. *AIMS Mater. Sci.* **2016**, *3*, 1054–1106. [[CrossRef](#)]
3. Aykol, M.; Kim, S.; Hegde, V.I.; Snyder, D.; Lu, Z.; Hao, S.; Kirklin, S.; Morgan, D.; Wolverton, C. High-throughput computational design of cathode coatings for Li-ion batteries. *Nat. Commun.* **2016**, *7*, 13779. [[CrossRef](#)] [[PubMed](#)]
4. Krttil, P.; Fattakhova, D. Li insertion into Li-Ti-O spinels: Voltammetric and electrochemical impedance spectroscopy study. *J. Electrochem. Soc.* **2001**, *148*, A1045–A1050. [[CrossRef](#)]
5. Pfanzell, M.; Kubiak, P.; Fleischhammer, M.; Wohlfahrt-Mehrens, M. TiO_2 rutile—An alternative anode material for safe lithium-ion batteries. *J. Power Sources* **2011**, *196*, 6815–6821. [[CrossRef](#)]
6. Guo, Y.-G.; Hu, Y.-S.; Sigle, W.; Maier, J. Superior electrode performance of nanostructured mesoporous TiO_2 (anatase) through efficient hierarchical mixed conducting networks. *Adv. Mater.* **2007**, *19*, 2087–2091. [[CrossRef](#)]
7. Armstrong, G.; Armstrong, A.R.; Bruce, P.G.; Reale, P.; Scrosati, B. $\text{TiO}_2(\text{B})$ nanowires as an improved anode material for lithium-ion batteries containing LiFePO_4 or $\text{LiNi}_{0.5}\text{Mn}_{1.5}\text{O}_4$ cathodes and a polymer electrolyte. *Adv. Mater.* **2006**, *18*, 2597–2600. [[CrossRef](#)]
8. Yang, J.; Zhao, J.; Chen, Y.; Li, Y. Preparation and characterization of LiTi_2O_4 anode material synthesized by one-step solid-state reaction. *Ionics* **2010**, *16*, 425–429. [[CrossRef](#)]
9. Ogihara, T.; Kodera, T. Synthesis of $\text{Li}_2\text{Ti}_3\text{O}_7$ anode materials by ultrasonic spray pyrolysis and their electrochemical properties. *Materials* **2013**, *6*, 2285–2294. [[CrossRef](#)]
10. Hong, Z.; Wei, M.; Ding, X.; Jiang, L.; Wei, K. $\text{Li}_2\text{ZnTi}_3\text{O}_8$ nanorods: A new anode material for lithium-ion battery. *Electrochem. Commun.* **2010**, *12*, 720–723. [[CrossRef](#)]
11. Zaghbi, K.; Simoneau, M.; Armand, M.; Gauthier, M. Electrochemical study of $\text{Li}_4\text{Ti}_5\text{O}_{12}$ as negative electrode for Li-ion polymer rechargeable batteries. *J. Power Sources* **1999**, *81–82*, 300–305. [[CrossRef](#)]
12. Han, J.-T.; Huang, Y.-H.; Goodenough, J.B. New anode framework for rechargeable lithium batteries. *Chem. Mater.* **2011**, *23*, 2027–2029. [[CrossRef](#)]

13. Gicquel, C.; Mayer, M.; Bouaziz, R. Diagramme de phase du système $\text{Li}_2\text{O}-\text{TiO}_2$. *C. R. Acad. Sci. Ser. C* **1972**, *275*, 1427–1430.
14. Izquierdo, G.; West, A.R. Phase equilibria in the system $\text{Li}_2\text{O}-\text{TiO}_2$. *Mater. Res. Bull.* **1980**, *15*, 1655–1660. [[CrossRef](#)]
15. Kleykamp, H. Enthalpy, heat capacity and enthalpy of transformation of Li_2TiO_3 . *J. Nucl. Mater. Sci.* **2001**, *43*, 244–248. [[CrossRef](#)]
16. Kleykamp, H. Phase equilibria in the Li-Ti-O system and physical properties of Li_2TiO_3 . *Fusion Eng. Des.* **2002**, *61*, 361–366. [[CrossRef](#)]
17. Laumann, A.; Fehr, K.T.; Wachsmann, M.; Holzapfel, M.; Iversen, B.B. Metastable formation of low temperature cubic Li_2TiO_3 under hydrothermal conditions—Its stability and structural properties. *Solid State Ion.* **2010**, *181*, 1525–1529. [[CrossRef](#)]
18. Lang, G. Die kristallstruktur einiger vertreter der verbindungsklasse $\text{Me}^{\text{I}}_2\text{Me}^{\text{IV}}\text{O}_3$ als beitrag zur aufklarung der ordnungsphase von Li_2TiO_3 . *Z. Anorg. Allg. Chem.* **1954**, *276*, 77–94. [[CrossRef](#)]
19. Kataoka, K.; Takahashi, Y.; Kijima, N.; Nagai, H.; Akimoto, J.; Idemoto, Y.; Ohshima, K.-I. Crystal growth and structure refinement of monoclinic Li_2TiO_3 . *Mater. Res. Bull.* **2009**, *44*, 168–172. [[CrossRef](#)]
20. Laumann, A.; Jensen, K.M.O.; Tyrsted, C.; Bremholm, M.; Fehr, K.T.; Holzapfel, M.; Iversen, B.B. In situ synchrotron X-ray diffraction study of the formation of cubic Li_2TiO_3 under hydrothermal conditions. *Eur. J. Inorg. Chem.* **2011**, *14*, 2221–2226. [[CrossRef](#)]
21. Ramaraghavulu, R.; Buddhudu, S.; Bhaskar-Kumar, G. Analysis of structural and thermal properties of Li_2TiO_3 ceramic powders. *Ceram. Int.* **2011**, *37*, 1245–1249. [[CrossRef](#)]
22. Dorrian, J.F.; Newnham, R.E. Refinement of the structure of Li_2TiO_3 . *Mater. Res. Bull.* **1969**, *4*, 179–183. [[CrossRef](#)]
23. Murphy, S.T.; Hine, N.D.M. Point defects and non-stoichiometry in Li_2TiO_3 . *Chem. Mater.* **2014**, *26*, 1629–1638. [[CrossRef](#)]
24. Castellanos, M.; West, A.R. Order-disorder phenomena in oxides with rock salt structures: The system $\text{Li}_2\text{TiO}_3-\text{MgO}$. *J. Mater. Sci.* **1979**, *14*, 450–454. [[CrossRef](#)]
25. Aguas, M.D.; Coombe, G.C.; Parkin, I.P. New solid-state routes to lithium transition metal oxides via reactions with lithium oxide. *Polyhedron* **1998**, *17*, 49–53. [[CrossRef](#)]
26. Bhaskar-Kumar, G.; Buddhudu, S. Synthesis and emission analysis of RE^{3+} (Eu^{3+} or Dy^{3+}): Li_2TiO_3 ceramics. *Ceram. Int.* **2009**, *35*, 521–525. [[CrossRef](#)]
27. Wu, X.; Wen, Z.; Lin, B.; Xu, X. Sol-gel synthesis and sintering of nano-size Li_2TiO_3 powder. *Mater. Lett.* **2008**, *62*, 837–839. [[CrossRef](#)]
28. Jung, C.H.; Park, J.Y.; Oh, S.J.; Park, H.K.; Kim, Y.S.; Kim, D.K.; Kim, J.H. Synthesis of Li_2TiO_3 ceramic breeder powders by the combustion process. *J. Nucl. Mater.* **1998**, *253*, 203–212. [[CrossRef](#)]
29. Sinha, A.; Nair, S.R.; Sinha, P.K. Single step synthesis of Li_2TiO_3 powder. *J. Nucl. Mater.* **2010**, *399*, 162–166. [[CrossRef](#)]
30. Jung, C.-H.; Lee, S.J.; Kriven, W.M.; Park, J.-Y.; Ryu, W.-S. A polymer solution technique for the synthesis of nano-sized Li_2TiO_3 ceramic breeder powders. *J. Nucl. Mater.* **2008**, *373*, 194–198. [[CrossRef](#)]
31. Zhang, L.; He, G.; Zhaou, D.; Zhou, J.; Yao, Q. Study on transformation mechanism of lithium titanate modified with hydrochloric acid. *Ionics* **2016**, *22*, 2007–2014. [[CrossRef](#)]
32. Ma, J.-L.; Fu, Z.-F.; Gao, J.; Zhang, X.-S. A simple method to synthesize nanosized Li_2TiO_3 powders through high-energy ball-milling. *Powder Metall. Met. Ceram.* **2015**, *54*, 410–415. [[CrossRef](#)]
33. Lulewicz, J.D.; Roux, N. Fabrication of Li_2TiO_3 pebbles by the extrusion-spheronisation-sintering process. *J. Nucl. Mater.* **2002**, *307*, 803–806. [[CrossRef](#)]
34. Wang, H.; Yang, M.; Gong, Y.; Feng, L.; Dang, C.; Shia, Y.; Shi, Q.; Wei, J.; Liao, Z.; Lu, T. Fabrication of nanostructured Li_2TiO_3 ceramic pebbles as tritium breeders using powder particles synthesized via a CTAB-assisted method. *Ceram. Int.* **2017**, *43*, 5680–5686. [[CrossRef](#)]
35. Miao, B.; Zeng, W.; Hussain, S.; Mei, Q.; Xu, S.; Zhang, H.; Li, Y. Large scale hydrothermal synthesis of monodisperse hexagonal WO_3 nanowire and the growth mechanism. *Mater. Lett.* **2015**, *147*, 12–15. [[CrossRef](#)]
36. Wan, Z.; Yu, Y.; Zhang, H.F.; Gao, T.; Chen, X.J.; Xiao, C.J. First-principles study of electronic, dynamical and thermodynamic properties of Li_2TiO_3 . *Eur. Phys. J. B* **2012**, *85*, 181–187. [[CrossRef](#)]

37. Fehr, T.; Schmidbauer, E. Electrical conductivity of Li_2TiO_3 ceramics. *Solid State Ion.* **2007**, *178*, 35–41. [[CrossRef](#)]
38. Dash, U.; Sahoo, S.; Chaudhuri, P.; Parashar, S.K.S.; Parashar, K. Electrical properties of bulk and nano Li_2TiO_3 ceramics: A comparative study. *J. Adv. Ceram.* **2014**, *3*, 89–97. [[CrossRef](#)]
39. Kim, J.-S.; Johnson, C.S.; Vaughey, J.T.; Thackeray, M.M.; Hackney, S.A.; Yoon, W.; Grey, C.P. Electrochemical and structural properties of $x\text{Li}_2\text{M}'\text{O}_3$ ($1-x$) $\text{LiMn}_{0.5}\text{Ni}_{0.5}\text{O}_2$ electrodes for lithium batteries ($\text{M}' = \text{Ti, Mn, Zr}$; $0 \leq x \leq 0.3$). *Chem. Mater.* **2004**, *16*, 1996–2006. [[CrossRef](#)]
40. Chauvaut, V.; Cassir, M. Behaviour of titanium species in molten $\text{Li}_2\text{CO}_3+\text{Na}_2\text{CO}_3$ and $\text{Li}_2\text{CO}_3+\text{K}_2\text{CO}_3$ in the anodic conditions used in molten carbonate fuel cells. II. Electrochemical intercalation of Li^+ in Li_2TiO_3 at 600 °C and 650 °C. *J. Electroanal. Chem.* **1999**, *474*, 9–15. [[CrossRef](#)]
41. Tabuchi, M.; Nakashima, A.; Shigemura, H.; Ado, K.; Kobayashi, H.; Sakaebe, H.; Tatsumi, K.; Kageyama, H.; Nakamura, T.; Kanno, R. Fine $\text{Li}_{(4-x)/3}\text{Ti}_{(2-2x)/3}\text{Fe}_x\text{O}_2$ ($0.18 \leq x \leq 0.67$) powder with cubic rock-salt structure as a positive electrode material for rechargeable lithium batteries. *J. Mater. Chem.* **2003**, *13*, 1747–1757. [[CrossRef](#)]
42. Shigemura, H.; Tabuchi, M.; Sakaebe, H.; Kobayashi, H.; Kageyama, H. Lithium extraction and insertion behavior of nanocrystalline Li_2TiO_3 - LiFeO_2 solid solution with cubic rock salt structure. *J. Electrochem. Soc.* **2003**, *150*, A638–A644. [[CrossRef](#)]
43. Morales, J.; Santos-Pena, J.; Trocoli, R.; Franger, S. Electrochemical activity of rock-salt-structured LiFeO_2 - $\text{Li}_{4/3}\text{Ti}_{2/3}\text{O}_2$ nanocomposites in lithium cells. *J. Nanopart. Res.* **2008**, *10*, 217–226. [[CrossRef](#)]
44. Shi, J.; Liang, Y.; Li, L.; Peng, Y.; Yang, H. Evaluation of the electrochemical characteristics of silicon/lithium titanate composite as anode material for lithium ion batteries. *Electrochim. Acta* **2015**, *155*, 125–131. [[CrossRef](#)]
45. Ko, Y.N.; Choi, S.H.; Kang, Y.C.; Park, S.B. Characteristics of Li_2TiO_3 - LiCrO_2 composite cathode powders prepared by ultrasonic spray pyrolysis. *J. Power Sources* **2013**, *244*, 336–343. [[CrossRef](#)]
46. Wang, Y.; Zhou, A.; Dai, X.; Geng, L.; Li, J.; Li, J. Solid-state synthesis of submicron-sized $\text{Li}_4\text{Ti}_5\text{O}_{12}/\text{Li}_2\text{TiO}_3$ composites with rich grain boundaries for lithium ion batteries. *J. Power Sources* **2014**, *266*, 114–120. [[CrossRef](#)]
47. Bhatti, H.S.; Anjum, D.; Ullah, S.; Ahmed, B.; Habib, A.; Karim, A.; Hasanain, S.K. Electrochemical characteristics and Li^+ ion intercalation kinetics of dual-phase $\text{Li}_4\text{Ti}_5\text{O}_{12}/\text{Li}_2\text{TiO}_3$ composite in the voltage range 0–3 V. *J. Phys. Chem. C* **2016**, *120*, 9553–9561. [[CrossRef](#)]
48. Lu, J.; Peng, Q.; Wang, W.; Nan, C.; Li, L.; Li, Y. Nanoscale coating of LiMO_2 ($\text{M} = \text{Ni, Co, Mn}$) nanobelts with Li^+ -conductive Li_2TiO_3 : toward better rate capabilities for Li-ion batteries. *J. Am. Chem. Soc.* **2013**, *135*, 1649–1652. [[CrossRef](#)] [[PubMed](#)]
49. Deng, H.; Nie, P.; Luo, H.; Zhang, Y.; Wang, J.; Zhang, X. Highly enhanced lithium storage capability of $\text{LiNi}_{0.5}\text{Mn}_{1.5}\text{O}_4$ by coating with Li_2TiO_3 for Li-ion batteries. *J. Mater. Chem. A* **2014**, *2*, 18256–18262. [[CrossRef](#)]
50. Jia, G.; Liu, S.; Yang, G.; Li, F.; Wu, K.; He, Z.; Shangguan, X. Effects of Li_2TiO_3 coating on the structure and the electrochemical properties of $\text{LiNi}_{0.5}\text{Mn}_{0.5}\text{O}_2$ cathode materials at high voltages. *Ionics* **2019**, *25*, 399–410. [[CrossRef](#)]
51. Zhao, E.; Liu, X.; Hu, Z.; Sun, L.; Xiao, X. Facile synthesis and enhanced electrochemical performances of Li_2TiO_3 -coated lithium-rich layered $\text{Li}_{1.13}\text{Ni}_{0.30}\text{Mn}_{0.57}\text{O}_2$ cathode materials for lithium-ion batteries. *J. Power Sources* **2015**, *294*, 141–149. [[CrossRef](#)]
52. Wang, J.; Yu, Y.; Li, B.; Fu, T.; Xie, D.; Cai, J.; Zhao, J. Improving the electrochemical properties of $\text{LiNi}_{0.5}\text{Co}_{0.2}\text{Mn}_{0.3}\text{O}_2$ at 4.6 V cutoff potential by surface coating with Li_2TiO_3 for lithium-ion batteries. *Phys. Chem. Chem. Phys.* **2015**, *17*, 32033–32043. [[CrossRef](#)] [[PubMed](#)]
53. Lakshmi-Narayana, A.; Dhananjaya, M.; Guru-Prakash, N.; Hussain, O.M.; Julien, C.M. Nanocrystalline Li_2TiO_3 electrodes for supercapattery application. *Ionics* **2017**, *23*, 3419–3428. [[CrossRef](#)]
54. Lakshmi-Narayana, A.; Dhananjaya, M.; Guru-Prakash, N.; Hussain, O.M.; Mauger, A.; Julien, C.M. $\text{Li}_2\text{TiO}_3/\text{graphene}$ and $\text{Li}_2\text{TiO}_3/\text{CNT}$ composites as anodes for high power Li-ion batteries. *ChemistrySelect* **2018**, *3*, 9150–9158. [[CrossRef](#)]
55. Hoshino, T.; Kawamura, H.; Dokiya, M.; Takahashi, Y.; Terai, T.; Yamawaki, M. Non-stoichiometry of Li_2TiO_3 under hydrogen atmosphere conditions. *J. Nucl. Mater.* **2004**, *329*, 1300–1304. [[CrossRef](#)]
56. Roisnel, T.; Rodriguez-Carjaval, J. WinPLOTR: A windows tool for powder diffraction pattern analysis. *Mater. Sci. Forum* **2001**, *378*, 118–123. [[CrossRef](#)]

57. Langford, J.I.; Wilson, A.J.C. Scherrer after sixty years: A survey and some new results in the determination of crystallite size. *J. Appl. Cryst.* **1978**, *11*, 102–113. [[CrossRef](#)]
58. Julien, C. Local cationic environment in lithium nickel-cobalt oxides used as cathode materials for lithium batteries. *Solid State Ion.* **2000**, *136*, 887–896. [[CrossRef](#)]
59. Bian, J.J.; Dong, Y.F. Sintering behavior, microstructure and microwave dielectric properties of $\text{Li}_{2+x}\text{TiO}_3$ ($0 \leq x \leq 0.2$). *Mater. Sci. Eng. B* **2011**, *176*, 147–151. [[CrossRef](#)]
60. Zhang, T.; Zuo, R.; Zhang, J. Structure, microwave dielectric properties and low-temperature sintering of acceptor/donor codoped $\text{Li}_2\text{Ti}_{1-x}(\text{Al}_{0.5}\text{Nb}_{0.5})_x\text{O}_3$ ceramics. *J. Am. Ceram. Soc.* **2016**, *99*, 825–832. [[CrossRef](#)]
61. Nakazawa, T.; Naito, A.; Aruga, T.; Grismanovs, V.; Chimi, Y. High energy heavy ion induced structural disorder in Li_2TiO_3 . *J. Nucl. Mater.* **2007**, *367*, 1398–1403. [[CrossRef](#)]
62. Mukai, K.; Kato, Y.; Nakano, H. Understanding the zero-strain lithium insertion scheme of $\text{Li}[\text{Li}_{1/3}\text{Ti}_{5/3}]\text{O}_4$: Structural changes at atomic scale clarified by Raman spectroscopy. *J. Phys. Chem. C* **2014**, *118*, 2992–2999. [[CrossRef](#)]
63. Denisova, T.A.; Maksimova, L.G.; Polyalov, E.V.; Zhuravlev, N.A.; Kovyazina, S.A.; Leonidova, O.N.; Khazbibulin, D.F.; Yureva, E.I. Metatitanic acid: Synthesis and properties. *Russ. J. Inorg. Chem.* **2006**, *51*, 691–699. [[CrossRef](#)]
64. Amalraj, F.; Markovsky, B.; Sharon, D.; Talianker, M.; Zinigrad, E.; Persky, R.; Haik, O.; Grinblat, J.; Lampert, J.; Schulz-Dobrick, M.; et al. Study of the electrochemical behavior of the “inactive” Li_2MnO_3 . *Electrochim. Acta* **2012**, *78*, 32–39. [[CrossRef](#)]
65. Julien, C.M.; Massot, M. Lattice vibrations of materials for lithium rechargeable batteries III Lithium manganese oxides. *Mater. Sci. Eng. B* **2003**, *100*, 69–78. [[CrossRef](#)]
66. Li, Z.; Du, F.; Bie, X.; Zhang, D.; Cai, Y.; Cui, X.; Wang, C.; Chen, G.; Wei, Y. Electrochemical kinetics of the $\text{Li}[\text{Li}_{0.23}\text{Co}_{0.3}\text{Mn}_{0.47}]\text{O}_2$ cathode material by GITT and EIS. *J. Phys. Chem. C* **2010**, *114*, 22751–22757. [[CrossRef](#)]
67. Yu, C.-L.; Yanagisawa, K.; Kamiya, S.; Kozawa, T.; Ueda, T. Monoclinic Li_2TiO_3 nano-particles via hydrothermal reaction: Processing and structure. *Ceram. Int.* **2014**, *40*, 1901–1908. [[CrossRef](#)]
68. Dash, U.; Sahoo, S.; Parashar, S.K.S.; Chaudhuri, P. Effect of Li^+ ion mobility on the grain boundary conductivity of Li_2TiO_3 nanoceramics. *J. Adv. Ceram.* **2014**, *3*, 98–108. [[CrossRef](#)]
69. Ngai, K.L.; Leon, C. Cage decay, near constant loss, and crossover to cooperative ion motion in ionic conductors: Insight from experimental data. *Phys. Rev. B* **2002**, *66*, 064308. [[CrossRef](#)]
70. Eddrief, M.; Dzwonkowski, P.; Julien, C.; Balkanski, M. The ac conductivity in $\text{B}_2\text{O}_3\text{-xLi}_2\text{O}$ films. *Solid State Ion.* **1991**, *45*, 77–82. [[CrossRef](#)]
71. Dzwonkowski, P.; Eddrief, M.; Julien, C.; Balkanski, M. Electrical a.c. conductivity of $\text{B}_2\text{O}_3\text{-xLi}_2\text{O}$ glass thin films and analysis using the electric modulus formalism. *Mater. Sci. Eng. B* **1991**, *8*, 193–200. [[CrossRef](#)]
72. Elliott, S.R. Temperature dependence of a.c. conductivity of chalcogenide glasses. *Philos. Mag. B* **1978**, *37*, 553–560. [[CrossRef](#)]
73. Jonscher, A.K. The universal dielectric response. *Nature* **1977**, *267*, 673–679. [[CrossRef](#)]
74. Vijayakumar, M.; Kerisit, S.; Yang, Z.G.; Graff, G.L.; Liu, J.; Sears, J.A.; Burton, S.D.; Rosso, K.M.; Hu, J.Z. Combined ^6Li NMR and molecular dynamics study of Li diffusion in Li_2TiO_3 . *J. Phys. Chem. C* **2009**, *113*, 20108–20116. [[CrossRef](#)]
75. Islam, M.M.; Bredow, T. Lithium diffusion pathways in $\beta\text{-Li}_2\text{TiO}_3$: A theoretical study. *J. Phys. Chem. C* **2016**, *120*, 7061–7066. [[CrossRef](#)]
76. Sun, X.; Hegde, M.; Zhang, Y.; He, M.; Gu, L.; Wang, Y.; Shu, J.; Radovanovic, P.V.; Cui, B. Structure and electrochemical properties of spinel $\text{Li}_4\text{Ti}_5\text{O}_{12}$ nanocomposites as anode for lithium-ion battery. *Int. J. Electrochem. Sci.* **2014**, *9*, 1583–1596.
77. Tang, S.B.; Lai, M.O.; Lu, L. Li-ion diffusion in highly (003) oriented LiCoO_2 thin film cathode prepared by pulsed laser deposition. *J. Alloys Compd.* **2008**, *449*, 300–303. [[CrossRef](#)]
78. Ho, C.; Raistrick, I.D.; Huggins, R.A. Application of a-c techniques to the study of lithium diffusion in tungsten trioxide thin films. *J. Electrochem. Soc.* **1980**, *127*, 343–350. [[CrossRef](#)]
79. Shi, Q.; Hu, R.; Zeng, M.; Zhu, M. A diffusion kinetics study of Li-ion in LiV_3O_8 thin film electrode. *Electrochim. Acta* **2010**, *55*, 6645–6650. [[CrossRef](#)]

80. Xie, J.; Tanaka, T.; Imanishi, N.; Matsumura, T.; Hirano, A.; Takeda, Y.; Yamamoto, O. Li-ion transport kinetics in LiMn_2O_4 thin films prepared by radio frequency magnetron sputtering. *J. Power Sources* **2008**, *180*, 576–581. [[CrossRef](#)]
81. Yang, X.; Yu, R.; Ge, L.; Wang, D.; Zhao, Q.; Wang, X.; Bai, Y.; Yuan, H.; Shu, H. Facile synthesis and performances of nanosized Li_2TiO_3 -based shell encapsulated $\text{LiMn}_{1/3}\text{Ni}_{1/3}\text{Co}_{1/3}\text{O}_2$ microspheres. *J. Mater. Chem. A* **2014**, *2*, 8362–8368. [[CrossRef](#)]
82. Kim, J.S.; Johnson, C.S.; Thackeray, M.M. Layered $x\text{LiMO}_2 \cdot (1-x)\text{Li}_2\text{M}'\text{O}_3$ electrodes for lithium batteries: A study of $0.95\text{LiMn}_{0.5}\text{Ni}_{0.5}\text{O}_2 \cdot 0.05\text{Li}_2\text{TiO}_3$. *Electrochem. Commun.* **2002**, *4*, 205–209. [[CrossRef](#)]
83. Zhang, L.Q.; Noguchi, H. Novel layered Li-Cr-Ti-O cathode materials related to the LiCrO_2 - Li_2TiO_3 solid solution. *J. Electrochem. Soc.* **2003**, *150*, A601–A607. [[CrossRef](#)]
84. Zhang, L.Q.; Wang, X.Q.; Noguchi, H.; Yoshio, M.; Takada, K.; Sasaki, T. Electrochemical and ex situ XRD investigations on $(1-x)\text{LiNiO}_2 \cdot x\text{Li}_2\text{TiO}_3$ ($0.05 \leq x \leq 0.5$). *Electrochim. Acta* **2004**, *49*, 3305–3311. [[CrossRef](#)]
85. Wu, X.W.; Wen, Z.Y.; Xu, X.G.; Han, J.D. Synthesis and ionic conductivity of Mg-doped Li_2TiO_3 . *Solid State Ion.* **2008**, *179*, 1779–1782. [[CrossRef](#)]
86. Wu, X.W.; Wen, Z.Y.; Wang, X.Y.; Xu, X.G.; Lin, J.; Song, S.F. Effect of Ta-doping on the ionic conductivity of lithium titanate. *Fusion Eng. Des.* **2010**, *85*, 1442–1445. [[CrossRef](#)]
87. Zhu, Y.R.; Yin, L.C.; Yi, T.F.; Liu, H.; Xie, Y.; Zhu, R.S. Electrochemical performance and lithium-ion intercalation kinetics of micron-sized $\text{Li}_4\text{Ti}_5\text{O}_{12}$ anode material. *J. Alloys Compd.* **2013**, *547*, 107–112. [[CrossRef](#)]
88. Li, S.; Guo, J.; Ma, Q.; Yang, Y.; Dong, X.; Yang, M.; Yu, W.; Wang, J.; Liu, G. Electrospun $\text{Li}_4\text{Ti}_5\text{O}_{12}/\text{Li}_2\text{TiO}_3$ composite nanofibers for enhanced high-rate lithium ion batteries. *J. Solid State Electrochem.* **2017**, *21*, 2779–2790. [[CrossRef](#)]
89. Ruprecht, B.; Wilkening, M.; Uecker, R.; Heitjans, P. Extremely slow Li ion dynamics in monoclinic Li_2TiO_3 —probing macroscopic jump diffusion via ^7Li NMR stimulated echoes. *Phys. Chem. Chem. Phys.* **2012**, *14*, 11974–11980. [[CrossRef](#)]
90. Vitins, G.; Kizane, G.; Lusic, A.; Tiliks, J. Electrical conductivity studies in the system Li_2TiO_3 - $\text{Li}_{1.33}\text{Ti}_{1.67}\text{O}_4$. *J. Solid State Electrochem.* **2002**, *6*, 311–319. [[CrossRef](#)]
91. Baklanova, Y.V.; Arapova, I.Y.; Shein, I.R.; Maksimova, L.G.; Mikhalev, K.N.; Denisova, T.A. Charge distribution and mobility of lithium ions in Li_2TiO_3 from $^6,7\text{Li}$ NMR data. *J. Struct. Chem.* **2013**, *54*, 111–118. [[CrossRef](#)]
92. Kuganathan, N.; Kordatos, A.; Fitzpatrick, M.E.; Vovk, R.V.; Chroneos, A. Defect process and lithium diffusion in Li_2TiO_3 . *Solid State Ion.* **2018**, *327*, 93–98. [[CrossRef](#)]
93. Ki, K.; Yang, W.; Wang, W.-H.; Li, Y.-T. First principles study of tritium diffusion in Li_2TiO_3 crystal with lithium vacancy. *Materials* **2018**, *11*, 2383.

